NIPPON STEEL TECHNICAL REPORT No. 135 MARCH 2026

Technical Report

Stainless Steel Plates That Contribute to Thermal Management

Atsutaka HAYASHI* Jun-ichi HAMADA
Tsuyoshi TAMOGAMI

Abstract

Electric vehicles (EV) are being increasingly used to achieve carbon neutrality; however, EV batteries heat up during use and fast charging, shortening their life. Thus, the batteries need to be cooled using refrigerants or coolants through a thermal management system. In this study, the heat exchange performances through aluminum or stainless steel plates with a thickness of 0.5–2 mm used as thermal management parts were evaluated. The heat exchange performance of stainless steel was almost the same as that of aluminum when the thicknesses of the plate was low, and it depended on the heat transfer because of water flow. Furthermore, stainless steel plates were superior to aluminum plates in terms of corrosion resistance in the SWAAT and pressure resistance in the cross-sectional shape of the stacked-plate heat exchanger. Stainless steel plates that have these superior properties can be used in a variety of environments, and contribute to thermal management components for EVs.

1. Introduction

The electrification of automobiles (electric vehicle [EV] adoption) is advancing toward a carbon-neutral society. One challenge for EVs is extending battery life, as heat generated during use, especially during rapid charging, shortens it.[1)] While air cooling was previously common for battery cooling, liquid-cooled thermal management components have been increasingly adopted in recent years.[2)] Thermal management components include radiators, stacked-plate-type heat exchangers that cool the coolant (long-life coolant [LLC]) using refrigerants, and battery coolers that cool battery modules using LLC. Aluminum alloys, known for their excellent thermal conductivity, are primarily used as materials for these components. On the other hand, the increasing diversity of refrigerant types and the need for higher cooling capacity[3, 4)] require higher material strength to accommodate the resulting higher internal pressures within components, as well as the trend toward thinner walls and more compact designs. Furthermore, corrosion resistance is required to withstand external salt-induced corrosion, and also to address variations in the Cl concentration and pH of LLC dilution water depending on the region of use.[5)] Stainless steel, which offers higher strength and superior corrosion resistance compared to aluminum alloys, has the challenge of having a thermal conductivity approximately one-tenth that of aluminum alloys. However, few reports have compared the heat exchange performance of stacked-plate-type heat exchangers and battery coolers using stainless steel.

In this study, the authors evaluated the effect of material plate thickness on heat exchange performance using stainless steel and aluminum alloy, assuming heat transfer in the direction of plate thickness, as in stacked-plate-type heat exchangers and battery coolers. The results clearly showed that when plate thickness is thin, the heat exchange performance of stainless steel and aluminum alloy is very similar. Furthermore, the corrosion resistance and pressure resistance of stainless steel and aluminum alloy were also evaluated, and these results are reported.

2. Evaluation of Heat Exchange Performance

2.1 Experimental method for heat exchange performance

Test specimens were 1 and 2 mm thick A1100 (pure aluminum alloy, thermal conductivity λ = 217 W °C^{-1} m^{-1}) and 0.5, 1, and 2 mm thick ferritic stainless steel SUS444 (Fe-19Cr-2Mo-0.5Nb, λ = 20.7 W °C^{-1} m^{-1}) and austenitic stainless steel SUS304L (Fe-18Cr-8Ni, λ = 14.7 W °C^{-1} m^{-1}). A schematic diagram of the heat exchange test is shown in **Fig. 1**. Heat was applied to the surface of the sample, conducted through the sample in the thickness direction via thermal

* Chief Manager, Head of Section, Research Section- I, Stainless Steel Research Dept.- I, Stainless Steel Research Lab., Steel Research Laboratories
3434 Ooaza-shimata, Hikari City, Yamaguchi Pref. 743-8550

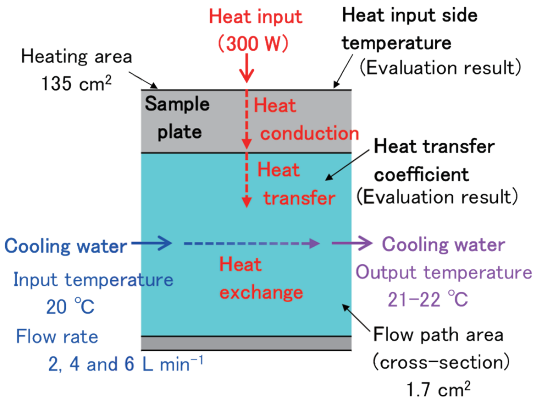

Fig. 1 Schematic of the heat exchange test

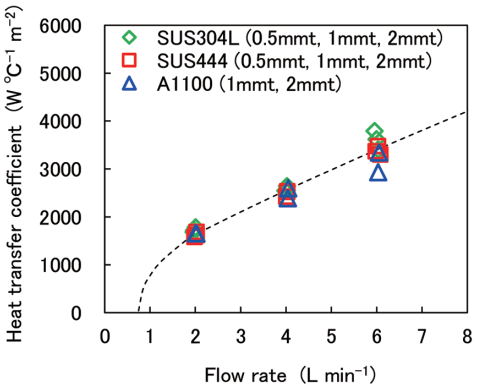

Fig. 2 Effect of flow rate on the heat transfer coefficient

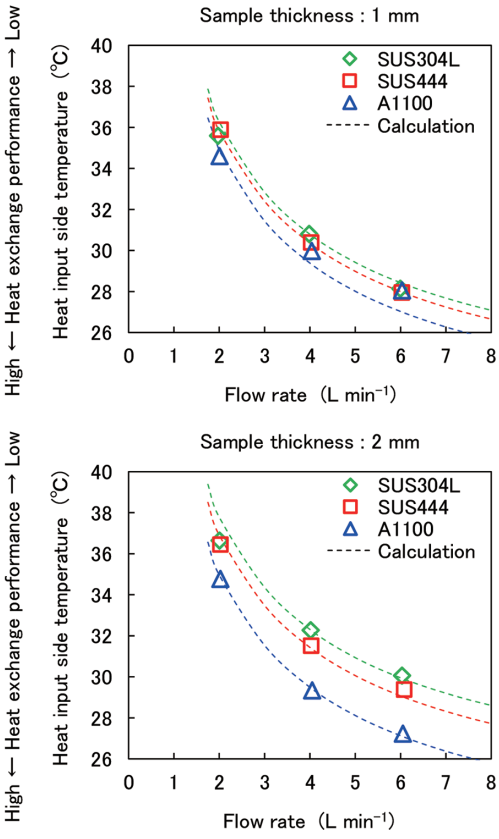

Fig. 3 Effect of flow rate on the heat exchange performance

conduction, transferred to the cooling water by heat transfer, and then dissipated externally as the cooling water flowed, thereby achieving heat exchange. The optimum temperature for lithium-ion batteries used in EVs is 15–35°C. In this test, the heat input side temperature was set to approximately 30–35°C. The heat input was 300 W, the cooling water temperature was 20°C, and the cooling water flow rate was 2, 4, and 6 L min^{-1} (flow velocity 0.2, 0.4, and 0.6 m sec^{-1}). The device dimensions were: heat transfer surface area 135 cm^2 (9.1 cm × 14.8 cm), cooling water flow channel cross-sectional area 1.7 cm^2 (1.4 cm × 1.2 cm). The flow channel was folded multiple times to ensure full contact with the entire heat transfer surface. From the measured temperatures at steady state after heat input, the heat input side temperature (lower temperatures indicate higher heat exchange performance) and heat transfer coefficient were determined.

The heat transfer calculation formula used in this test is shown below. The formula accounts for the effects of slight variations in heat input and cooling water input temperature that occur experimentally. Predicted values of the heat input side temperature were also calculated for each condition.

Heat input : $Q1 = 300$ (W) (1)

Heat conduction : $Q2 = \lambda \times (T^M_{In} - T^M_{Out}) \times S/t$ (2)

Heat transfer : $Q3 = h \times S \times \Delta Tm$ (3)

$$\Delta Tm = (T^W_{Out} - T^W_{In}) / Ln\left((T^M_{Out} - T^W_{In})/(T^M_{Out} - T^W_{Out})\right)$$

Heat exchange : $Q4 = (T^W_{Out} - T^W_{In}) \times \rho \times Cp \times A \times v$ (4)

Steady-state condition : $Q1 = Q2 = Q3 = Q4$ (5)

λ: Thermal conductivity (W °C^{-1} m^{-1}), T^M_{In}: Heat input side temperature (°C), T^M_{Out}: Cooling side temperature (°C), S: Heating area (m^2), t: Plate thickness (m), h: Heat transfer coefficient (W °C^{-1} m^{-2}), ΔTm: Logarithmic mean temperature difference (°C), T^W_{In}: Cooling water input temperature (°C), T^W_{Out}: Cooling water output temperature (°C), ρ: Density of cooling water (kg m^{-3}), Cp: Specific heat of cooling water (J kg^{-1} °C^{-1}), A: Flow path cross-sectional area (m^2), v: Cooling water flow velocity (m sec^{-1})

2.2 Evaluation results of heat exchange performance

Figure 2 shows the relationship between cooling water flow rate and heat transfer coefficient. The heat transfer coefficient is equivalent between materials and depends on the cooling water flow rate. As the cooling water flow rate increases to 2, 4, and 6 L min^{-1}, the heat transfer coefficient improves to approximately 1 700, 2 500, and 3 400 W °C^{-1} m^{-2}, respectively.

Figure 3 shows the relationship between cooling water flow rate and heat input side temperature for plate thicknesses of 1 mmt and 2 mmt. The heat input side temperature decreases as the cooling water flow rate increases, indicating a trend toward improved heat exchange performance. This is influenced by the increase in heat transfer coefficient shown in Fig. 2. The heat input side temperature for each material follows the trend: (low) A1100 < SUS444 < SUS304L (high). Materials with higher thermal conductivity exhibit lower heat input side temperatures and higher heat exchange performance. Comparing the effects of material (thermal conductivity) and cooling water flow rate (heat transfer), the cooling water flow rate has a greater influence. The calculated values generally agree with the experimental results. Using these calculations, it can be seen that even with SUS304L, which has a thermal conductivity approximately 1/15th that of A1100, increasing the cooling water flow rate by

about 1.5 times results in an equivalent heat input side temperature.

Figure 4 shows the relationship between plate thickness and heat input side temperature at cooling water flow rates of 2, 4, and 6 L min^{-1}. Materials with lower thermal conductivity tend to exhibit higher heat input side temperatures. Conversely, reducing plate thickness lowers the heat input side temperature, diminishing the difference between materials. Particularly at a plate thickness of 0.5 mm, the heat input side temperatures for SUS444 and SUS304L do not align with their thermal conductivity values, showing only a slight difference within the experimental error range. The calculated values generally agree with the experimental results. For a plate thickness of 0.5 mm, the difference in heat input side temperature between A1100 and SUS304L is calculated to be only 0.7°C.

Based on these results, for stacked-plate-type heat exchangers or

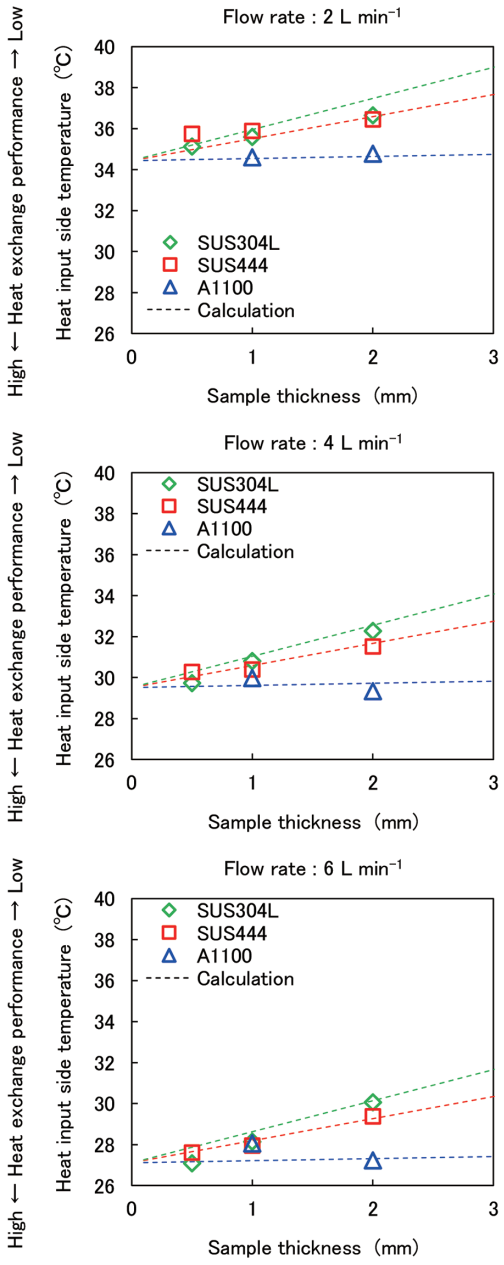

Fig. 4 Effect of sample thickness on the heat exchange performance

battery coolers where heat transfer occurs in the plate thickness direction, increasing the cooling water flow rate or reducing the plate thickness would make the heat exchange performance of aluminum alloy and stainless steel nearly equivalent.

In this test, the heat transfer coefficient improved with increased cooling water flow rate, and its impact on heat exchange performance was greater than that of the material's thermal conductivity. Furthermore, with thinner plate thicknesses, the difference between materials became negligible. These findings were examined by understanding the boundary layer that affects the heat transfer coefficient and calculating its thickness.

Just beneath the material wall in the flow path, fluid viscosity causes friction between the fluid and the material surface, forming a region where flow velocity decreases. This region is called the boundary layer. The temperature near the material wall is close to the material temperature, creating a temperature gradient toward the center of the flow path. When the cooling water flow velocity increases, the boundary layer becomes thinner, as if being swept away, which promotes heat transfer and improves the heat transfer coefficient.

Fluid flow can be either laminar or turbulent, and the boundary layer itself can also be laminar or turbulent, independent of the main flow. The distinction between laminar and turbulent flow is determined using the Reynolds number (Re), expressed by Equation (6).

$$Re = v \times L / \nu \quad (6)$$

[6]

L = 2 × short side × long side / (short side + long side) (For rectangular tubes)

v: Cooling water flow velocity (m sec^{-1}),

L: Characteristic length (m) = Hydraulic diameter,

ν: Kinematic viscosity coefficient of cooling water = 1 × 10^{-6} (at 20°C)

The main flow Reynolds number indicates laminar flow for Re < 2 300 and turbulent flow for Re > 4 000.[7] The boundary layer Reynolds number indicates a laminar boundary layer for Re < 500 000 and a turbulent boundary layer for Re > 500 000.[8] In this experiment, Re values for cooling water flow rates of 2, 4, and 6 L min^{-1} were 2 897, 5 841, and 8 725, respectively. The main flow falls within the turbulent regime, transitioning from the laminar region, while the boundary layers remain laminar in all cases. Let y be the distance from the material surface at which the boundary layer velocity u reaches 99% of the main flow velocity U. Approximating the velocity distribution in the laminar boundary layer as $u = a + by + cy^2$, solving the boundary layer Equation[9] yields Equation (7) as the formula for calculating the laminar boundary layer thickness δ (m).

$$\delta = 5.48 \times (\nu \times L/v)\ 0.5 = 5.48 \times L \times Re^{-0.5} \quad (7)$$

Figure 5 shows the results of calculating the relationship between cooling water flow rate and boundary layer thickness in this experiment using Equation (7). The boundary layer becomes thinner as the cooling water flow rate increases, at flow rates of 2, 4, and 6 L min^{-1}, it becomes 1.5, 1.1, and 0.9 mm, respectively. Since the material plate thickness ranges from 0.5 to 2 mm, and the boundary layer thickness is comparable to the plate thickness, it cannot be neglected. Furthermore, the thermal conductivities of A1100, SUS444, SUS304L, and water are 217, 20.7, 14.7, and 0.5 W °C^{-1} m^{-1}, respectively, with that of water being two orders of magnitude lower than those of the materials. Therefore, heat transfer through the boundary layer is considered to have a significant impact on heat exchange performance. **Figure 6** shows the relationship between cooling water flow rate and heat transfer coefficient (as shown in Fig. 2), converted using Equation (7) into the relationship between

boundary layer thickness and heat transfer coefficient. As the cooling water flow rate increases, the boundary layer thickness decrease, leading to a significant improvement in the heat transfer coefficient. This explains why the cooling water flow rate had a major effect in this experiment. Furthermore, for the thin 0.5 mm plate, the boundary layer thickness exceeds the plate thickness. Consequently, the heat exchange performance is limited by the heat transfer coefficient, and the influence of the material's thermal conductivity is considered to be minimal.

3. Corrosion Resistance Evaluation

3.1 Corrosion resistance test method

The test specimens included aluminum alloys A3003 (Al-Mn alloy) and A7075 (Al-Zn-Mg alloy), and stainless steels SUH409L (Fe-11Cr-0.2Ti, PREN=11), SUS430LX (Fe-17Cr-0.2Ti, PREN=17), SUS436L (Fe-17Cr-1Mo-0.2Ti, PREN=21), and SUS444 (Fe-18Cr-2Mo-0.5Nb, PREN=25). Note that PREN is calculated as Cr + 3.3Mo (mass%). Test specimens measuring 70 mm × 150 mm with a P600 wet-ground surface finish were prepared from these materials and subjected to the SWAAT test (Sea Water Acidified Test, ASTM G85-A3), a corrosion test for aluminum alloys. The SWAAT test is a cyclic corrosion test consisting of spraying (49°C, artificial seawater + acetic acid solution, pH 2.8–3.0, 30 min) and wetting (49°C, 98% RH, 90 min). Observation of appearance, corrosion loss, and maximum corrosion depth were measured after 168 cycles and 336 cycles of the SWAAT test.

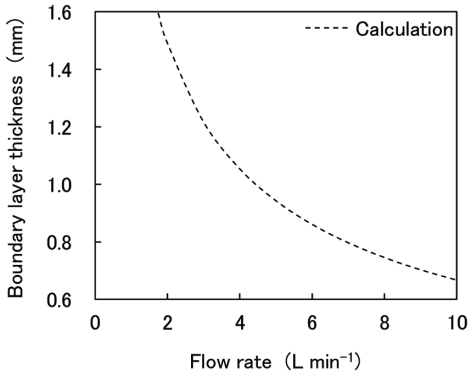

Fig. 5 Effect of flow rate on boundary layer thickness

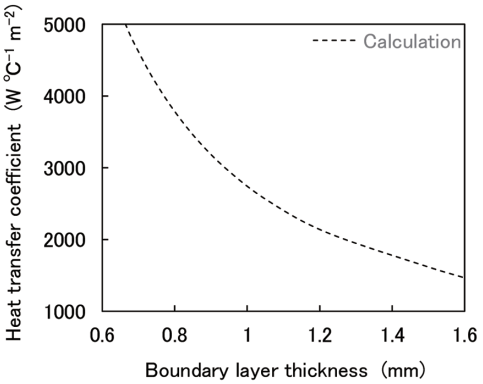

Fig. 6 Effect of boundary layer thickness on the heat transfer coefficient

3.2 Corrosion resistance evaluation results

Figure 7 shows the appearance, maximum corrosion depth, and corrosion loss of each test specimen after the SWAAT test. Although the rust on the aluminum alloy is white and not very noticeable, the mottled appearance in the photographs indicates significant corrosion. Among the stainless steels, SUH409L exhibited severe corrosion, while the others showed only minor corrosion. Furthermore, the corrosion loss followed the trend: (high) SUH409L > A7075 > A3003 > SUS430LX, SUS436L, SUS444 (small). The maximum corrosion depth followed the trend: (large) SUH409L ≈ A7075 > A3003 > SUS430LX > SUS436L > SUS444 (small). **Figure 8** shows SEM images of pitting corrosion on SUS430LX and A3003. Compared to SUS430LX, the pit on A3003 exhibited a more irregular shape and significantly greater corrosion.

Assuming weight loss due to corrosion follows a linear law, the calculated weight loss rates are shown in **Fig. 9**. For stainless steel, the weight loss rate decreased with increasing PREN, and when PREN ≥ 17, it became at least one order of magnitude lower than that of the aluminum alloys.

Regarding corrosion depth, assuming a parabolic law due to decelerated corrosion over time, the calculated corrosion depth progression rates are shown in **Fig. 10**. For stainless steel, the corrosion depth progression rate decreased with increasing PREN, and when PREN ≥ 17, it was more than one order of magnitude lower than that of the Al alloys.

	A 7075	A 3003	SUH 409L	SUS 430LX	SUS 436L	SUS 444
168cyc						
D (mm)	0.51	0.41	0.54	0.045	0.033	No pit
W (mg cm^{-2})	3.8	0.5	7.3	<0.1	<0.1	<0.1
336cyc						
D (mm)	0.80	0.63	0.83	No pit	0.026	No pit
W (mg cm^{-2})	6.5	1.5	10.8	<0.1	<0.1	<0.1

D : Maximum corrosion depth, W : Corrosion weight loss

Fig. 7 Appearance of the specimens after the SWAAT

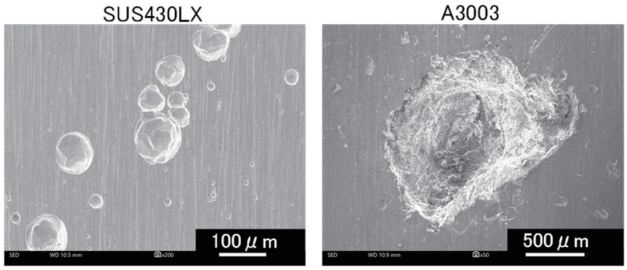

Fig. 8 Appearance of the corrosion pits after the SWAAT

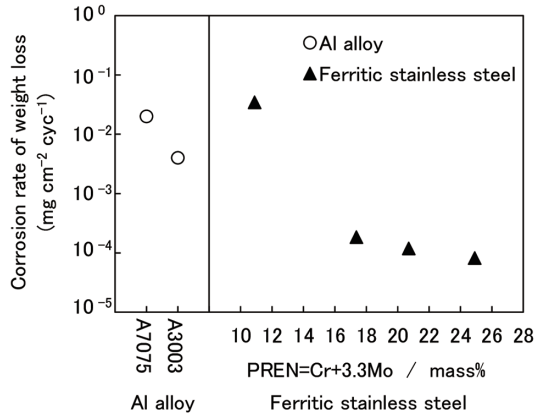

Fig. 9 Corrosion rate of weight loss calculated using the linear law in the SWAAT

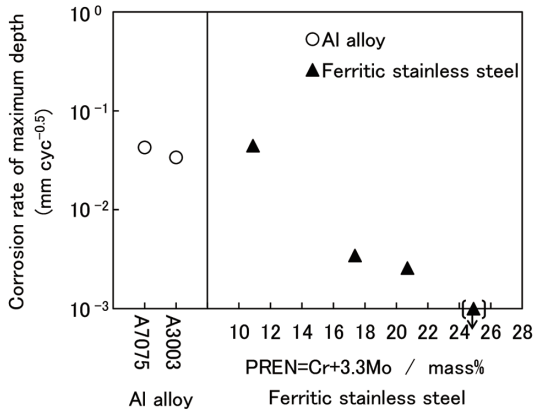

Fig. 10 Corrosion rate of the maximum depth calculated using the parabolic law in the SWAAT

As described above, stainless steel with PREN ≥ 17 exhibits significantly superior corrosion resistance compared to aluminum alloys. However, aluminum alloys can be used in clad structures, where a zinc-containing aluminum alloy serves as a sacrificial protective layer. In this study, a clad plate consisting of an A3003 core material (plate thickness: 0.25 mm) and an A7075 sacrificial layer (plate thickness: 0.05 mm) was considered. Based on the weight loss rate in Fig. 9, the number of cycles required for the entire 0.05 mm sacrificial layer to be consumed was estimated to be 668 cycles. Subsequently, using the corrosion depth progression rate from Fig. 10, the total number of cycles required for pitting corrosion to penetrate the A3003 core was estimated to be 730 cycles. The corrosion depth of the stainless steel at 730 cycles, calculated using the corrosion depth progression rate in Fig. 10, is shown in **Fig. 11**. For SUS 430LX (PREN=17), the estimated corrosion depth at 730 cycles was 0.09 mm. This indicates that, for an aluminum alloy with a sacrificial protective layer and a total plate thickness of 0.3 mm, stainless steel with PREN ≥ 17 is expected to exhibit comparable pitting corrosion resistance in the SWAAT test, even with the plate thickness is reduced to one-third.

4. Evaluation of Pressure Resistance

4.1 Pressure resistance analysis method

To evaluate pressure resistance, deformation under varying refrigerant pressure was simulated using a configuration representing a stacked-plate-type heat exchanger. **Figure 12** shows a schematic of the heat exchanger cross-section, modeled as a half-symmetrical shape in a two-dimensional model (MARC, finite element method). Material data included the stress-strain curve (Young's modulus: 70 GPa, 0.2% proof stress: 23 MPa) for A3003 (Al-Mn alloy) subjected to brazing-simulated heat treatment at 600°C for 5 minutes, and the stress-strain curve for SUS430J1L (Fe-18.5Cr-0.4Cu-0.4Nb) subjected to brazing-simulated heat treatment at 1 130°C for 10 minutes (Young's modulus: 210 GPa, 0.2% proof stress: 292 MPa). The pressure in the cooling fluid flow path was kept constant at 0.1 MPa, and the deformation of the corrugated fins was simulated by increasing the pressure in the refrigerant flow path. Simulations were also performed for plate and corrugated fin thicknesses reduced to one-third and doubled, respectively, to calculate the refrigerant pressure at which plastic strain occurs in the corrugated fins.

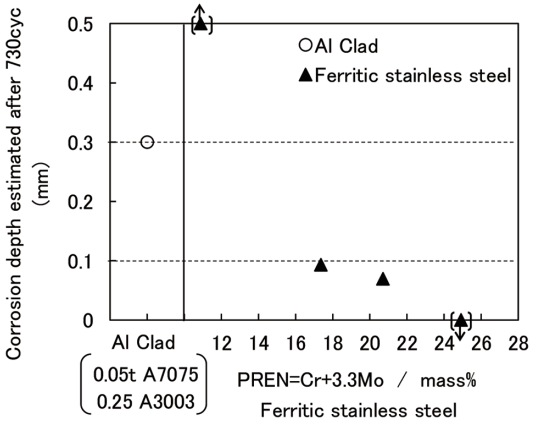

Fig. 11 Corrosion depth calculated after 730 cyc in the SWAAT

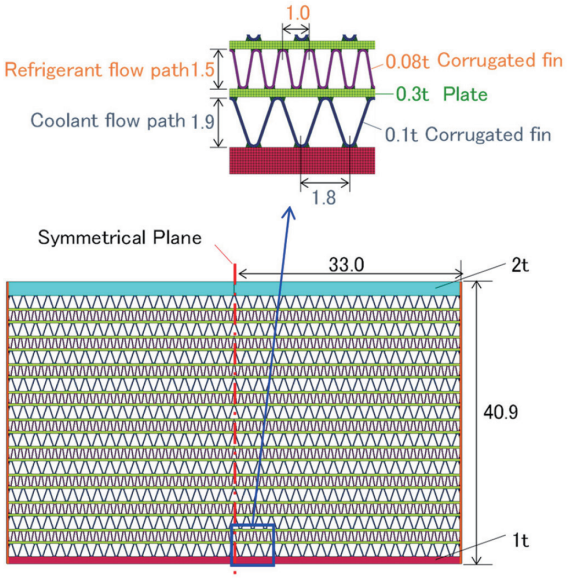

Fig. 12 Schematic of the two-dimensional model for the pressure resistance simulation of the plate-type heat exchanger

4.2 Pressure resistance evaluation results

Figure 13 shows a contour plot of the equivalent plastic strain of

A3003 at a refrigerant pressure of 10 MPa as an example of the simulation results. The refrigerant flow path expands vertically at the center and deforms outward in all directions at the sides. Furthermore, the plastic strain is concentrated in the corrugated fins with thinner plate thickness. **Figure 14** shows the relationship between refrigerant pressure and the plastic strain in the corrugated fins of the refrigerant flow path. For A3003, plastic strain begins to increase at approximately 4 MPa, while for SUS430J1L, it starts increasing at approximately 40 MPa. Based on these results, the pressure resistance of SUS430J1L is estimated to be about 10 times greater than that of A3003, likely due to its higher strength. **Figure 15** shows the relationship between the thickness of the plate and corrugated fins and the refrigerant pressure at which plastic strain occurs in the corrugated fins. SUS430J1L exhibits plastic strain at higher pressures than A3003. Using a 0.3 mm-thick plate and 0.08 mm-thick corrugated fin made of A3003 as a reference, SUS 430J1L is considered to have equivalent or higher pressure resistance even at one-third the plate thickness. Furthermore, the refrigerant pressure at which plastic strain occurs is proportional to the plate thickness. For example, if six times the pressure resistance of the A3003 standard is required, A3003 would need to increase the plate thickness by a factor of six. In contrast, SUS430J1L is expected to maintain sufficient pressure resistance at its standard plate thickness and accommodate higher internal pressures within components[3, 4] corresponding to refrigerant type and cooling capacity.

5. Conclusion

This study evaluated the heat exchange performance, corrosion resistance, and pressure resistance of aluminum alloys and stainless steel for thermal management components, yielding the following results.

(1) Heat exchange performance improved as plate thickness decreased, and the difference between materials became smaller. At 0.5 mm thickness, the difference between the aluminum alloy and stainless steel was negligible.

(2) Corrosion resistance evaluation using the SWAAT test showed that stainless steels (SUS430LX, SUS436L, SUS444) with PREN (Cr + 3.3Mo) ≥ 17 exhibited corrosion weight loss and corrosion depth more than one order of magnitude lower than A3003, demonstrating excellent corrosion resistance.

(3) Simulation of pressure resistance based on the cross-sectional shape of a stacked-plate-type heat exchanger indicated that the refrigerant pressure causing plastic deformation in corrugated fins was approximately 10 times higher for SUS430J1L than for A3003, demonstrating superior pressure resistance for stainless steel.

Based on the above results, it is considered that stainless steel, not just aluminum alloys, is applicable for thin-walled thermal management components. Furthermore, the use of stainless steel enables thinner walls, compact designs, higher pressure resistance, and component use in diverse regions with varying corrosion environments, contributing to EV thermal management.

References

1) Kawawada, T., Watanabe, R.: Deterioration Restraint of Lithium-ion Battery for EV by Cooling in Charge. Transactions of Society of Automotive Engineers of Japan. 47 (1), 133–137 (2016)

2) Zhang, Li: Investigation report about cooling methods of electric vehicle batteries. Central Research Institute of Electric Power Industry Report. Tokyo, Central Research Institute of Electric Power Industry, 2020, 22p

3) Hara, J. et al.: CO_2 Refrigerant Air Conditioners, Automotive Thermal

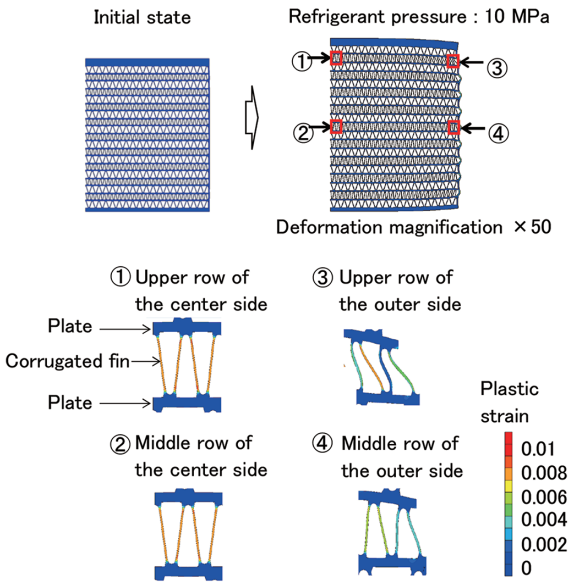

Fig. 13 **Plastic strain contour map for the heat exchanger made of A3003 at 10 MPa refrigerant pressure**

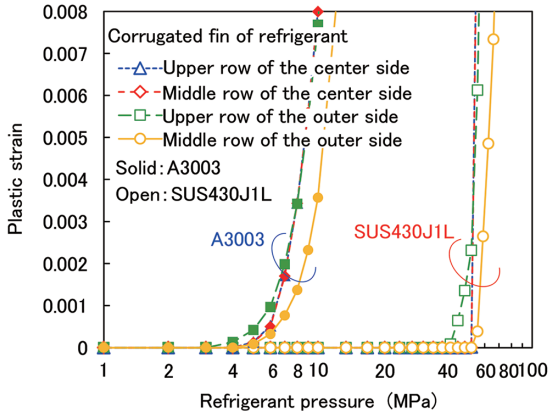

Fig. 14 **Effect of refrigerant pressure on the plastic strain of corrugated fins made of A3003 and SUS430J1L**

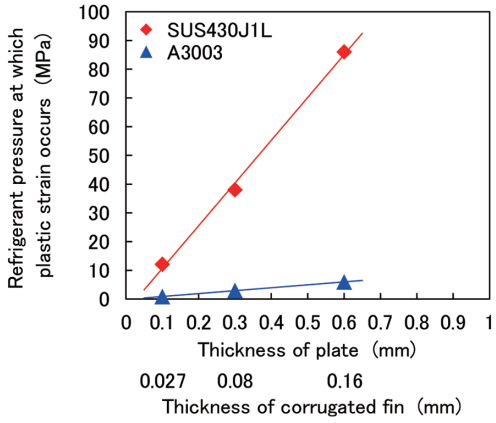

Fig. 15 **Effect of refrigerant pressure at which plastic strain occurs on the thickness of plates and corrugated fins**

Management and Air Conditioning Technology. Tokyo, Science & Technology, 2019, p. 333–341
4) Adachi, T., Uehara, H.: Pressure drop and heat transfer of flow in channels with periodically grooved parts. Proceedings of the 13th Computational Mechanics Conference, Japan Society of Mechanical Engineers. 2000, p. 139–140
5) Ando, Y., Nita, I., Uramoto, M., Ochiai, H., Fujiyoshi, T.: Development of Aluminum Radiators Using the Nocolok Brazing Process - Corrosion Resistance of New Aluminum Radiators by Applying a Nocolok Brazing Process. SAE Technical Paper, 1987, 1987-02-870180, doi:10.4271/870180
6) Japan Society of Mechanical Engineers: Heat Transfer Handbook. Tokyo, Maruzen, 1993, 429p
7) Jack Philip Holman: Heat Transfer. New York, McGraw-Hill, 2002, 665p
8) Frank P. Incropera, David P. DeWitt: Fundamentals of Heat and Mass Transfer, New York, Wiley, 1990, 992p
9) Asano, K.: Fundamentals and Applications of Mass Transfer. Tokyo, Maruzen, 2004, 274p

This paper is a reprint of “Evaluation of heat exchanging performances through aluminum or stainless steel plates for thermal management parts,” originally published in the Technical Sessions Proceedings of the Society of Automotive Engineers of Japan Academic Conference, 2024 Autumn Congress, Presentation No. 124, Document No. 20246124, with some additions.

Atsutaka HAYASHI
Chief Manager, Head of Section
Research Section-I, Stainless Steel Research Dept.-I
Stainless Steel Research Lab.
Steel Research Laboratories
3434 Ooaza-shimata, Hikari City, Yamaguchi Pref.
743-8550

Jun-ichi HAMADA
Dr.Eng., General Manager, Head of Lab.
Stainless Steel Research Lab.
Steel Research Laboratories

Tsuyoshi TAMOGAMI
Senior Manager
Battery & Electronic Material Evaluation Dept.
Electronic Material Solution Div.
R&D Supporting Unit
Nippon Steel Technology Co., Ltd.